J. T. Dobbins III, et. al.. "Medical Imaging."

Medical Imaging

James T. Dobbins III
Duke University Medical Center

Sean M. Hames
Duke University Medical Center

Bruce H. Hasegawa
University of California, San Francisco

Timothy R. DeGrado
Duke University Medical Center

James A. Zagzebski
University of Wisconsin, Madison

Richard Frayne
University of Wisconsin, Madison

79.1   Introduction

Medical imaging has advanced considerably since the discovery of X-rays by Wilhelm Conrad Röntgen in 1895. Today, in addition to the continued use of X-rays for medical diagnosis, there are imaging methods that use sound (ultrasound), magnetic fields and radio waves (magnetic resonance imaging), and radionuclides (nuclear medicine). Both projection imaging and cross-sectional imaging are routinely used clinically. This chapter will describe the principles behind the various imaging modalities currently in use, and the various measurements routinely made with them.

79.2   Image Information Content

The vast majority of imaging procedures are qualitative in nature, where it is the visual presentation of anatomy that is the measurement outcome. There are also some quantitative measurements, which will be discussed in the section on nuclear medicine. However, since most imaging is concerned only with the qualitative nature of the image, a description of the salient features of image content follows.

There are three primary physical parameters of interest in image content: contrast, noise, and resolution. If these three features are known for a given image (or imaging system), then the entire physical nature of the image has been characterized. There are also psychovisual effects, such as conspicuity [1],

which affect the ability of the observer to detect a particular feature, but these issues are difficult to quantitate and are outside the scope of this handbook.

The first of the physical image features, contrast, is defined as the fraction of the total image signal occupied by a particular object:

$$C = \frac{B-S}{B} \tag{79.1}$$

where S is the signal in the area of interest and B is the background signal. Contrast is determined by the properties of the object being imaged, the imaging modality, the properties of the image detector, postprocessing of the image (such as by digital processing), and the contrast of the display device.

Image noise is a measure of the stochastic nature of the image. All physical measurements, including medical images, contain a certain degree of uncertainty. In X-ray imaging, for example, the physics of X-ray production dictates that the number of X-rays incident on a unit area per unit time are random, and given by a statistical distribution known as the Poisson distribution. The greater the image noise, the less likely it is that one will observe a given object. There is a relationship between the image noise, the contrast and area of an object, and its likelihood of being observed. This is summarized in the Rose model:

$$N = \frac{k^2}{C^2 A} \tag{79.2}$$

where N is the number of quanta (such as X-rays) per unit area needed to discern an object of contrast C and area A, assuming a signal-to-noise of k. Rose found that a signal-to-noise ratio of 5 is typically required to detect a visual object reliably [2].

Resolution is the ability of an imaging system to record faithfully the range of spatial detail in an object. Recording objects with finer spatial detail requires "sharper" imaging detectors. The resolving ability of a detector is largely determined by its point-spread function. The point-spread function describes how well the imaging apparatus can record an infinitesimal point object. No detector is perfectly sharp, and some spread of the infinitesimal dot occurs — the worse the spread, the less resolving the system.

Measurement of Imaging Performance

A linear-systems approach is typically used to quantify the performance of an imaging system. The relations among contrast, noise, and resolution of an imaging system are customarily described by two functions: the modulation transfer function (MTF) and the noise power spectrum (NPS), both of which are functions of spatial frequency. The MTF is the Fourier transform of the point-spread function, and describes the inherent deterministic frequency response of the system. The NPS (also referred to as the Wiener spectrum) is proportional to the square of the Fourier transform amplitude at each frequency, and represents the variance associated with noise in the system at each particular spatial frequency. The ratio of MTF and NPS, properly normalized, is the noise equivalent quanta (NEQ), which is the square of the maximum available signal-to-noise at each spatial frequency u:

$$NEQ(u) \equiv \frac{\left(\text{large area signal}\right)^2 \cdot \text{MTF}^2(u)}{\text{NPS}(u)} \tag{79.3}$$

If the NEQ is divided by the number of incident quanta per area (e.g., the number of X-ray photons incident on the detector in X-ray imaging), the result is the detective quantum efficiency (DQE). The

zero-frequency DQE is a measure of the fraction of incident quanta effectively used by the system. Alternatively, the DQE may be viewed as the efficiency with which the system utilizes the available signal-to-noise at each spatial frequency.

The actual measurement of MTF, NPS, and DQE is quite tedious, and will be only briefly summarized here. The interested reader is encouraged to consult the suggested references for the appropriate detail on these measurements. Examples of these measurements will be given for X-ray imaging.

The MTF is typically measured by imaging either a very fine slit (typically 10 to 20 μm) [3-6] or an edge [7]. The profile across the slit image is called the line-spread function (LSF). The Fourier transform of the LSF gives the MTF in the direction perpendicular to the slit. The derivative of values along the edge-response function also gives the line-spread function. Detector response typically varies with energy so it is important to specify the conditions under which MTF is measured. With X-ray imaging it is typical to use a tube voltage of 70 kV with 0.5 mm Cu filtration placed in the beam to simulate the filtering of the X-ray spectrum expected from a patient, although other measurement techniques are also found in the literature.

The NPS is measured by taking an image of a flat field, where there is no structure in the image other than noise. Contemporary methods of NPS measurement on digital systems perform a two-dimensional Fourier transform on the flat-field image [6], although when measuring the NPS of film a scanning slit is used to generate a one-dimensional NPS parallel to the direction of slit movement [8-10]. After appropriate scaling, the square of the amplitude of the two-dimensional Fourier transform is the NPS. There are many details related to measuring the NPS properly, including eliminating background trends, and the size of the region over which the Fourier transform is taken. These are all covered in detail in the references [6,8-18].

Measurement of imaging properties is easier on digital imaging systems than on film, since film must first be digitized at appropriately fine sampling intervals or else corrected for the use of one-dimensional slits [19]. However, the effects of aliasing (fictitious frequency response in a digital system due to limited sampling) makes the interpretation of MTF and NPS in digital systems more difficult than with film [11,12,20].

79.3   X-Ray Imaging

X-ray imaging requires an X-ray-generating apparatus (tube, high voltage supply, and controls) and an appropriate X-ray detector. Typical X-ray detectors include photographic film (almost always used in concert with a fluorescent screen), image intensifiers, computed radiography phosphor plates, and newer dedicated digital detectors.

The X-ray generator is basically a high-voltage step-up transformer with appropriate rectification and control circuitry. Most contemporary generators are three-phase 12-pulse, full-wave rectified to give a very low voltage ripple (3 to 10%) [21]. For procedures requiring very fast pulses of several milliseconds or less (such as coronary angiography), a tetrode-based constant-potential generator is used. The operator selects the tube kilovoltage, tube current, and exposure time appropriate for the examination of interest.

X-ray tubes contain a heated filament (which serves as the cathode) and an anode made of a tungsten/rhenium combination for conventional use or molybdenum for mammography. With the exception of dental tubes, modern clinical X-ray tubes almost always contain a rotating anode to spread the heat out over a larger area, allowing for a greater tube output without damaging the anode. Many tubes contain two filaments, a large one and a small one, depending on tube output and resolution requirements of a particular exam. Measurements on X-ray tubes and generators involve calibrations to assure that kilovoltage, tube output, and exposure time are in good agreement with the control console settings [21]. Calibration of the high voltage is done by commercially available voltage dividers, or by specially designed X-ray film cassettes with calibrating filters inside. Tube output is measured by ion chambers, and exposure time is measured either by a rotating-arm timer test tool placed over a film cassette during an X-ray exposure or by direct plotting of the exposure vs. time output of an ion chamber.

X-Ray Imaging Detectors

The most common detector for X-ray imaging is film. X-ray film is typically placed in a sandwich between two fluorescent screens (or one screen in mammography for improved visibility of small detail). Contemporary screens are made of rare earth compounds such as Gd_2O_2S, and serve to convert the X-rays to visible light which exposes the film more efficiently than X-rays alone, thus reducing patient radiation dose. The response of these screen–film combinations has good contrast at intermediate exposure ranges (as given by the film γ, or contrast ratio), but poor contrast at low or high exposures. The contrast and latitude of films are described by the characteristic curve (often referred to as the Hurter–Driffield, or HD curve). Appropriate screen–film combinations are chosen based on the anatomy to be imaged, since screen–film combinations are designed with different contrast, latitude, and exposure sensitivity characteristics [22].

A second type of X-ray detector is the image intensifier, which is used with fluoroscopy. Fluoroscopy uses a low-exposure-rate X-ray output to image a patient continuously, typically to properly position the patient for a subsequent high-exposure film image. The image intensifier (Figure 79.1) comprises a cylindrical glass enclosure, inside of which is an input screen, photocathode, focusing electrodes, accelerating anode, and output screen [21]. The X-rays are absorbed in the input screen (typically CsI), giving off light which liberates electrons from the photocathode. The photoelectrons are then accelerated to the output screen where they strike the output phosphor screen with high energy (~30 keV), giving off a bright light, which is viewed by either a video camera or motion-picture (cineradiographic) camera.

A recently developed digital X-ray detector is the photostimulable phosphor, which is referred to commonly as computed radiography [23-25]. This detector uses a special type of phosphor which stores about half of the absorbed X-ray energy in metastable states, which are read out later by laser scanning. The laser light stimulates the phosphor to emit ultraviolet light in proportion to the original X-ray exposure. The photostimulated light is then detected with a photomultiplier tube (PMT) or solid-state photodetector and digitized. The clinical apparatus (Figure 79.2) first does a prescan of the imaging plate to adjust the input range of the analog-to-digital converter based on the image histogram; the digitized signal is then logarithmically transformed and stored, displayed on a video monitor, or printed on film following optional spatial filtering and contrast adjustment.

There are also currently available or in development a variety of other digital X-ray detectors, including selenium plate detectors [26], CCD-camera detectors with fluorescent screens [27], and flat-panel arrays with amorphous silicon [28] or amorphous selenium [29] detector elements.

79.4 Computed Tomography

A diagnostic computed tomography (CT) scanner comprises an X-ray tube with collimation to provide the slice thickness, a linear array of detector elements, and a reconstruction computer. The X-ray tube and the detectors typically rotate in a gantry. The number of detectors used depends on the generation of the scanner. First-generation scanners had only one detector which was translated across the patient with the tube for each projection, and then the entire assembly was rotated to acquire the next projection view. To increase acquisition speed, second-generation scanners used several detectors in a limited fan-beam geometry. Third-generation CT scanners, which are the most common in use today, utilize a large fan array of detectors (852 elements in a current scanner), which completely encompasses the patient and allows slice acquisition times of about 1 s [21]. The X-ray tube and the detector fan array are mechanically coupled and rotate together at high speed (Figure 79.3).

The implementation of electronic slip rings, which allow continuous electric contact, has removed the physical restriction imposed by the high-voltage cables of earlier scanners. Fourth- and fifth-generation scanners have a stationary, complete ring of detectors (typically 1200 to 4800 detectors). In fourth-generation scanners the X-ray tube is rotated alone, while the fifth-generation scanner design has a focused electron beam which traverses multiple target rings. Fifth-generation scanners can acquire a slice
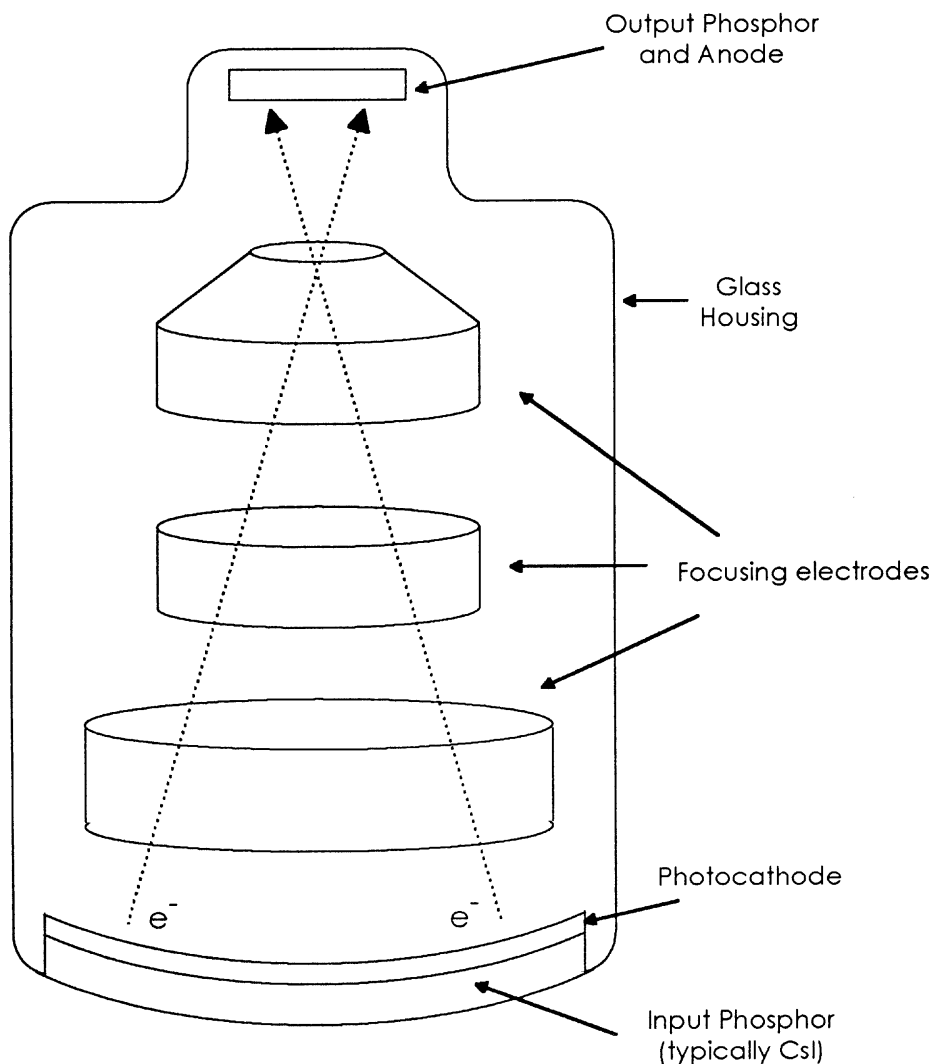
FIGURE 79.1 Schematic diagram of the major components of an image intensifier. The anode is typically at about 30 kV, and the three annular electrodes focus the beam and determine the usable area of the input surface for intensifiers having multiple formats.

fast enough (50 ms per slice and 17 slices per second) to stop cardiac motion [30,31]. These last two generations are not in common use, primarily due to high cost. In recent years, a helical-scan adaptation of third-generation scanners, allowing continuous acquisition of data over a large patient volume, has become clinically popular [32,33].

While the X-ray tubes used for CT (tube potential range 80 to 140 kV) are very similar to general radiographic tubes, the detectors are quite different from conventional radiographic detectors. Detectors used in CT are one-dimensional photon counters which must be efficient and fast. Early CT devices used scintillation detectors, which converted the X-ray energy into light photons that were counted by PMTs. Originally, single-crystal NaI was used, but it proved to be insufficient in dynamic range and had too much afterglow of scintillation light. High-pressure (25 atm) xenon gas later replaced NaI as the detector. Currently, many CT scanners use scintillating ceramics (e.g., $CdWO_4$, $(Y,Gd)_2O_3:Eu$ and $Gd_2O_2S:Pr,Ce$) coupled to photodiodes, due to the high bulk density of the ceramics.
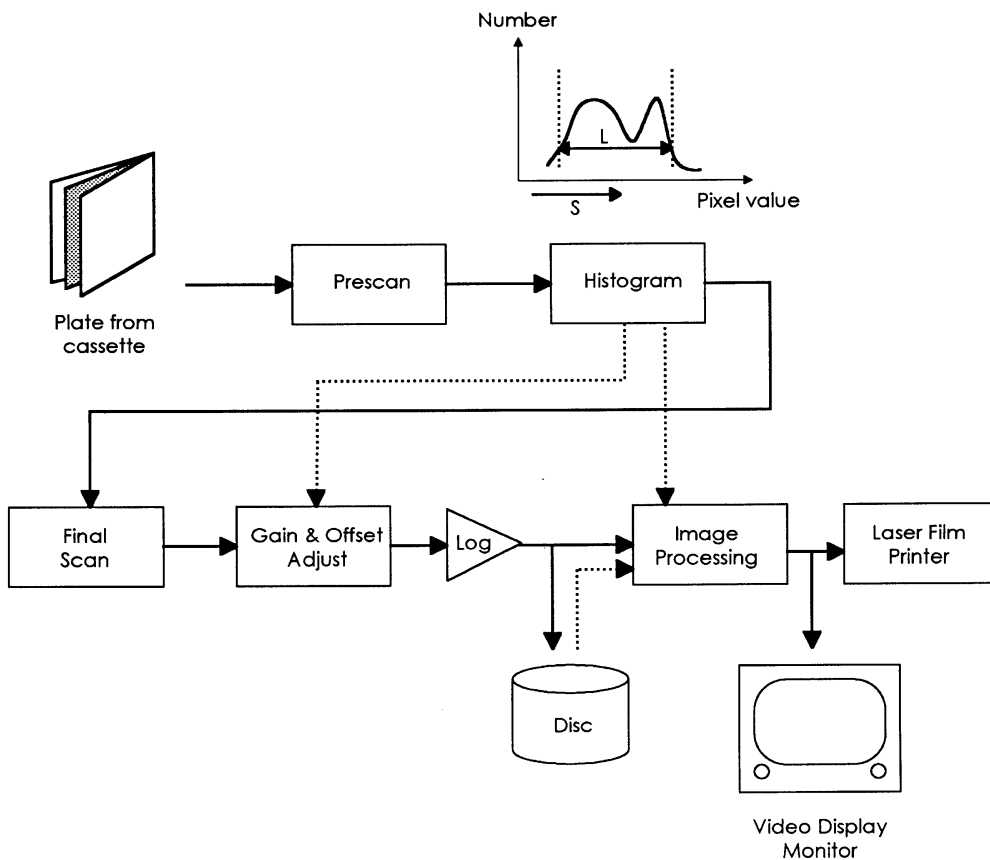
FIGURE 79.2 Schematic diagram of a typical photostimulable phosphor computed radiography system.

Reconstruction of an Object from Projections

CT is based on the image reconstruction theorem, which states that if one measures enough projections of an object, the two-dimensional distribution of that object may be reconstructed from the projection data. In CT the quantity of interest is the linear attenuation coefficient, μ, at each point in the object. The transmission of X-rays through an object of thickness x can be stated as

$$I\left(x\right) = I\left(0\right)e^{-\mu x} \tag{79.4}$$

where $I(0)$ is the incident intensity. Each ray from the focal spot of the tube to a discrete detector element is a measure of the line integral of the attenuation coefficient through the patient:

$$\lambda\left(x_{\mathrm{r}}\right) = -\ln\frac{I\left(x_{\mathrm{r}}\right)}{I\left(0\right)} = \int_{\ell}\mu\left(x_{\mathrm{r}}, y_{\mathrm{r}}\right)dy_{\mathrm{r}} \tag{79.5}$$

where r represents the reference frame of one of the many projections through the patient.

Image reconstruction requires a method to invert Equation 79.5, in order to extract $\mu(x,y)$ of the object from the measured projection views, λ. The mathematical principles of image reconstruction from an
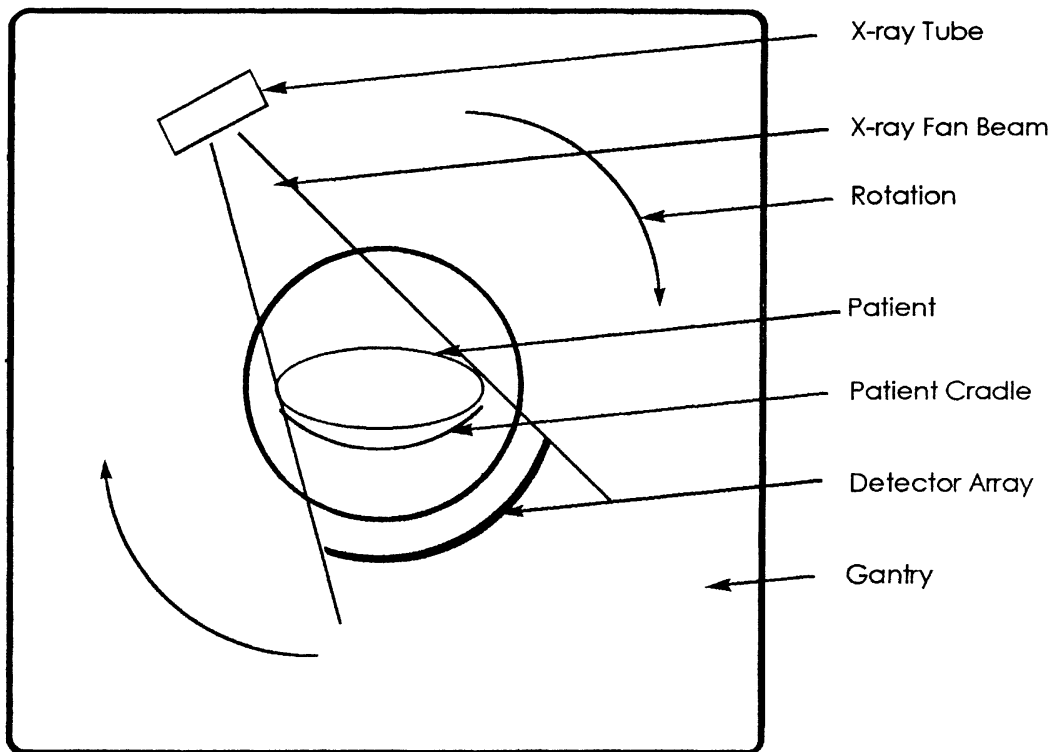
FIGURE 79.3 Orientation of components in a typical third-generation CT scanner.

infinite number of projections through an object were developed by Radon in 1917 [34]. An approximate solution to the Radon inversion, known as backprojection, was later developed because of the need for rapid computation of images in clinical CT. Backprojection involves smearing the data from each projection through the two-dimensional space of the patient, and summing over all projections. Simple backprojection yields an estimate of the patient structures, but is plagued by artifacts due to the approximate nature of the reconstruction procedure. These artifacts are successfully removed, however, by prefiltering the projection data before backprojecting. The one-dimensional prefiltering is typically performed in frequency space by multiplying by a ramp function. This technique is known as filtered backprojection, and results in more accurate reconstructions of patient anatomy [35].

There are several conditions that can reduce the quality of image reconstruction. First, an insufficient number of angular projections or incomplete sampling of the object can lead to aliasing in the reconstructed view. Second, partial volume effects occur when the object is not of homogeneous composition in a particular voxel, causing the reconstructed pixel value (CT number) to be not representative of the tissue. Third, if the acquisition is not fast enough, patient motion leads to a ghosting artifact in the reconstructed image. Last, beam hardening occurs when a high-density structure, such as the skull, significantly changes the beam energy spectrum. The result is reduced intensity of adjacent structures. Beam hardening can be reduced by slightly altering the shape of the reconstruction filter to improve the reconstruction for a particular tissue type.

To present the reconstructed data in digital format, the CT number (also known as the Hounsfield unit, HU) was developed.

$$\text{CT number} \equiv 1000 \times \frac{\mu_{\text{pixel}} - \mu_{\text{water}}}{\mu_{\text{water}}} \tag{79.6}$$

Using this normalization, pixel values in a CT image are stored as 12-bit integers between –1000 and 3095. A pixel containing only water would have a CT number equal to 0, while one containing bone or muscle would have a positive value and one with only fat or air would have a negative value.

Clinical Measurements

The reconstructed images are only as accurate as the data input to the algorithm; therefore, a rigorous calibration and quality assurance program is vital to the performance of a diagnostic CT scanner. Calibration generates a baseline reference in air for the scanner and calibration values for every possible scan parameter. Detector channel variation and interaction, along with X-ray tube focal spot size and position are quantified. A phantom is used to measure detector response for typical beam widths (1, 3, 5, 7, and 10 mm) and tube potentials (80, 100, 120, and 140 kV). The positioning accuracy of the scanner is also checked.

Quality assurance seeks to establish and maintain consistent image quality [36,37]. A specialized Plexiglas phantom is used to monitor the low-contrast detectability and high-contrast resolution and noise characteristics of the system. The low-contrast portion of the phantom consists of a set of holes of different diameter in a thin polystyrene slab. The 0.75-mm-thick polystyrene, when submerged in water and scanned with a 10 mm slice thickness, yields low contrast in the holes of about 1% (10 HU). The minimum detectable diameter is then found. The high-contrast resolution part of the phantom contains several repeating, equally sized bar/space patterns (spaces filled with water, contrast ~12% or 120 HU) with bar widths from 0.5 to 1.6 mm. The MTF is computed as a plot of the high-contrast frequency response [38]. The noise and uniformity of the scan are assessed with a homogeneous section of the phantom. An ROI is placed in the homogeneous area and the standard deviation is calculated, which should be approximately 3 HU.

79.5 Nuclear Medicine

Nuclear medicine techniques [39,40] use radiopharmaceuticals which are injected into the body to monitor or measure physiological function. Central to nuclear medicine is the role of the radiopharmaceutical as a tracer, that is, an agent with a predictable physiological action that is introduced without perturbing the function of the system. An external detector is used to record radioactivity emanating from the patient to determine the spatial distribution (and often temporal changes in concentration) of the radiopharmaceuticals in specific organs or tissues. Each radiopharmaceutical has an expected bio-distribution which a radiologist evaluates to diagnose the medical status of a patient. The radiopharmaceutical can be labeled either with positron-emitting radionuclides, which produce annihilation photons, or can be labeled with "single-photon" radionuclides which emit γ-rays (or sometimes X-rays). This section considers only single-photon-emitting radionuclides, examples of which are given in Table 79.1.

The scintillation camera [41,42] is the most common device for imaging the distribution of single-photon emitting radionuclides *in vivo* (Figure 79.4). The scintillation camera incorporates a large-field (e.g., 40 by 50 cm) position-sensitive photon detector with a collimator having a large number of small parallel holes (1 to 2 mm diameter, 4 cm length) so that only photons traveling perpendicular to the detector surface are recorded. Photons emitted by the patient and passing through the collimator are absorbed by a 1-cm-thick sodium iodide scintillator coupled to an array of PMTs. The PMT signals are processed to generate signals proportional to the (x,y)-coordinates of the interaction site of the photon in the crystal. In addition, the photomultiplier tube signals are integrated to calculate the photon energy. Events falling within a specified range (typically ±7.5%) around the expected radionuclide photon energy are recorded, whereas those outside of this range are rejected as unwanted scatter or background events. An image is integrated from individual events at the calculated position and specified energy, representing detected photons emitted by the radiopharmaceutical. The camera acquires a planar projection image of the radiopharmaceutical distribution in the patient with a spatial resolution of about 1 cm. The image also can be acquired tomographically by rotating the scintillation camera around the axis of the patient.

TABLE 79.1 Examples of Tracers Used in Nuclear Medicine

| Process	Tracer	Ref.
Blood Flow		
Diffusible	^{133}Xe	57
	[^{99m}Tc]-HMPAO	58
Diffusible (trapped)	[^{123}I]IMP (brain)	58
	^{201}Tl (heart),	44,59
	[^{99m}Tc]-MIBI	47
Nondiffusible (trapped)	[^{99m}Tc]macroaggregated albumin, labeled microspheres	—
Effective renal plasma flow	[^{123}I]hippuran	—
Blood Volume		
Red blood cells (RBC)	[^{99m}Tc]-RBC	45,46
Plasma	[^{125}I]-albumin	—
Transport and Metabolism		
Free fatty acids	[^{123}I]-hexadecanoic acid	44
Bile	[^{99m}Tc]-HIDA	—
Osteoblastic activity	[^{99m}Tc]-MDP	43
Glomerular filtration rate	[^{99m}Tc]-DPTA	60
Molecular Diffusion	[^{99m}TcO$_4$]	58
Receptor Systems		
Dopaminergic	[^{123}I]-IBZM	61
Cholinergic	[^{123}I]-QNB	62
Adrenergic	[^{131}I]-MIBG	63,64
Somatostatin	[^{111}In]-octreotide	65,66

Adapted from Sorenson and Phelps.[42]

This technique is called single-photon emission computed tomography (SPECT) and produces cross-sectional images representing the radiopharmaceutical concentration within the patient.

Measurement of Physiological Function

Radionuclide images can be interpreted visually or quantitatively. For example, the radiopharmaceutical [^{99m}Tc]-methylene diphosphonate (MDP) is incorporated into the bone matrix by osteoblastic activity [43]. A radiologist will inspect a nuclear medicine image for sites demonstrating focal uptake of ^{99m}Tc-MDP to determine the extent and degree of trauma, inflammation, degeneration, metastatic disease, or other skeletal disease processes. Typically, ^{99m}Tc-MDP images are interpreted visually but are not analyzed to determine the quantity of radiotracer incorporated into the skeleton.

Other nuclear medicine studies are assessed quantitatively in the sense that values extracted from the image represent the radioactivity concentration (and physiological function) in a specific organ or tissue region. Myocardial perfusion imaging with [^{99m}Tc]-hexatris-2-methoxyisobutylisonitrile (MIBI) is an example of one such "quantitative" nuclear medicine study for assessing a patient suspected of having coronary artery disease [44-46]. [^{99m}Tc]-MIBI is a lipophilic cation which accumulates in myocardial tissue roughly in proportion to blood flow [47]. Image data are acquired using SPECT to reconstruct tomograms of the myocardial concentration of [^{99m}Tc]-MIBI which are analyzed to assess regional myocardial blood flow. Although absolute measurements (μCi/g) of tissue activity are difficult (if not impossible) to obtain with SPECT, the images are interpreted "quantitatively" by extracting pixel values from the image to derive diagnostic information [48], rather than relying on "qualitative" visual interpretation of the images. Typically, ^{99m}Tc-MIBI is imaged in the "short-axis" view which presents the left ventricular myocardium in a series of annuli (or "doughnuts"). The image is analyzed using a "circumferential profile" representing the radionuclide concentration at 6° angular increments around each annular slice of the myocardium [49]. The extracted values are compared with standard values obtained from patients in whom atherosclerotic disease has been excluded by coronary angiography, thereby
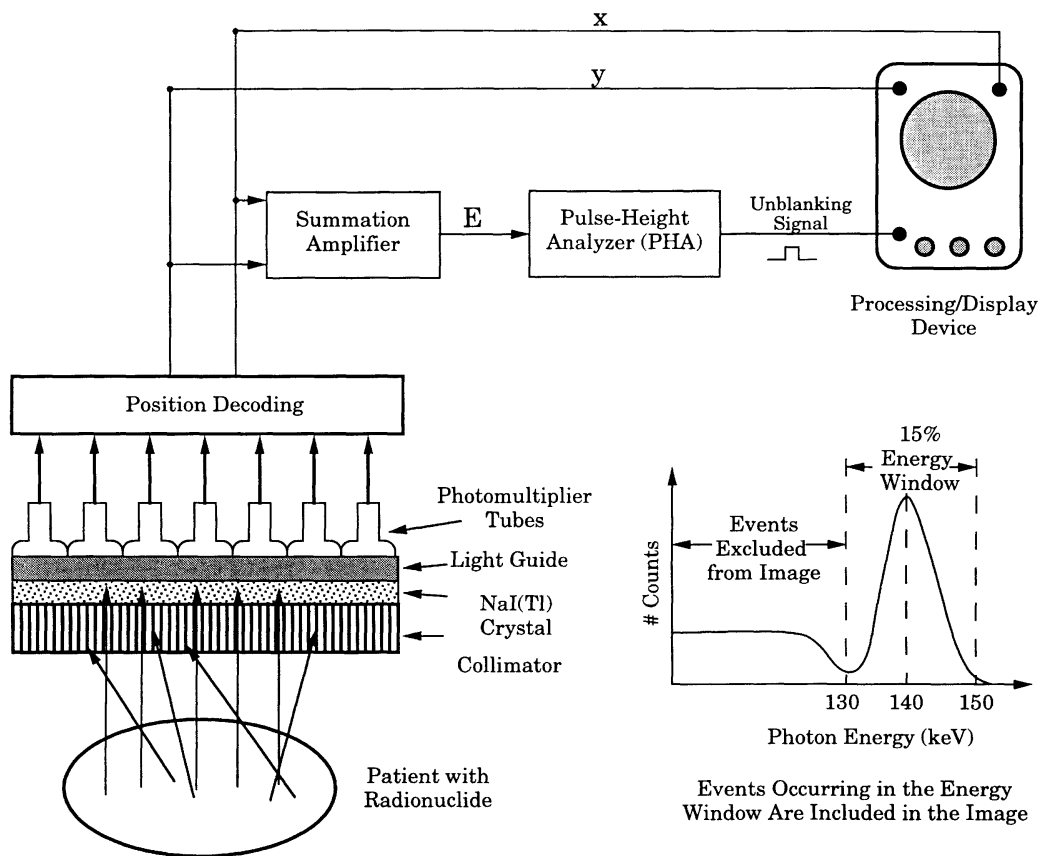
FIGURE 79.4 Scintillation camera incorporates collimator, scintillation crystal, photomultiplier tubes, and electronic circuitry to generate position (x,y) and energy (E) of photons emitted by radiopharmaceutical distribution in patient. Only events falling within a specified energy window are recorded by the processing or display device to form the nuclear medicine image.

allowing the nuclear cardiologist to assess both the presence as well as the regional extent of coronary artery disease.

Measurement of Technical Performance

Several parameters generally are measured to assess the performance of the scintillation camera [50-56]. *Spatial resolution* represents the precision with which the position of an event is localized, and can be assessed from the full-width at half-maximum (FWHM) of a profile taken across the image of a point or linear radioactive object having small dimensions in comparison to the resolution of the system. *Spatial linearity* is quantified as the accuracy with which the position of an event is localized, and represents the ability of a scintillation camera to produce a straight image of a straight object. Spatial linearity is measured as the deviation about the best-fit line in an image of a parallel line phantom or a orthogonal hole phantom, expressed as a percentage (ideally less than 1%) of the detector diameter. *Energy resolution* represents the precision with which the energy of a photon is recorded and generally is measured as the FWHM of the photopeak in an energy spectrum (number of detected photons recorded as a function of photon energy) of the radioactive source. *Flood field uniformity* assesses the ability of the camera to record a spatially uniform image when presented with a spatially uniform distribution of photons. An intrinsic measurement is performed by irradiating the uncollimated detector with the point source placed

at a distance equal to at least five times the field of view of the detector. The system uniformity can be checked by irradiating the entire surface of a collimated detector with an extended source of uniform radioactivity. *Sensitivity* represents the number of photons recorded per unit of source radioactivity when the detector is operated either without (intrinsic sensitivity) or with (extrinsic sensitivity) a collimator. *Count-rate linearity* represents the ability of the camera to record a count rate proportional to the photon event rate received by the detector. At low event rates, the measured count rate increases linearly with the actual photon event rate. Because the scintillation camera acts as a paralyzable system, at higher event rates, the measured count rate is lower than that predicted from linear response. At sufficiently high event rates, the measured count rate actually can decrease with increasing photon event rate and eventually can be extinguished when imaging radioactive sources of sufficiently high activities.

79.6   Positron Emission Tomography (PET)

PET involves a physiological administration of a positron-emitting radiopharmaceutical into the human body. The principal advantage of PET over single-photon imaging is the availability of a number of physiologically relevant radiotracers that are labeled with the short-lived positron-emitting radionuclides ^{11}C ($T_{1/2} = 20.4$ min), ^{13}N (9.96 min), ^{15}O (2.04 min), and ^{18}F (109.8 min). A typical PET center consists of a cyclotron for on-site isotope production, a radiochemistry laboratory for synthetic incorporation of the isotopes into organic molecules, and a PET scanner. PET instrumentation is described in detail in several review articles [67,68].

Principle of Coincidence Detection

The proton-rich radioisotopes used with PET imaging undergo β-decay, and emit positrons (antielectrons). A positron travels a short distance and combines with an electron from the surrounding medium. The masses of the positron and electron are converted to electromagnetic radiation in the form of two γ rays of energy 511 keV, which are emitted at nearly 180° to each other. The PET scanner utilizes multiple opposing γ detectors that surround the positron emitter, each defining a linear volume of response between the detectors. Coincidence timing circuitry enables effective localization of the decay events occurring between detector pairs, rejecting events in each detector that originate from outside the volume of response. A typical modern PET scanner employs tens of thousands of small detectors (or analogous position-coded larger detectors), yielding as many as tens of millions of such volumes of response. The coincidence principle is also utilized to measure and correct for attenuation of photons within the body, allowing the measurement of radioactivity concentration in absolute terms (i.e., Bq/mL). In this case, a separate "transmission" measurement scan is performed, using an external positron-emitting source placed adjacent to the subject yet within the volume of response. A "blank" scan is similarly acquired but without the subject in the field of view. The ratio of coincident count rates in the blank/transmission scans multiplies the corresponding coincidence counts in the emission scan to correct for attenuation along each coincidence line of response.

Detector Composition

The choice of detector material for PET scanners is influenced by a number of considerations, including scanner geometry, detection efficiency (stopping power), output signal strength (energy resolution), signal decay time (count rate capability), physical stability (i.e., hygroscopicity), availability, and cost. Inorganic scintillators are best suited for detection of the 511 keV photons. The physical properties of the two most widely used scintillators, NaI(Tl) and bismuth germanate (BGO), are shown in Table 79.2. NaI(Tl) has found application in position-sensitive detector systems that utilize a small number of large crystals observed by multiple PMTs. NaI(Tl) offers the advantages of (1) good energy resolution for effective rejection of scattered radiation, (2) good timing resolution for minimizing the coincidence-resolving time window, (3) availability of large crystals, and (4) relatively low cost. The higher stopping

TABLE 79.2 Physical Properties of Scintillators
Commonly Employed in PET Scanners

	NaI(Tl)	BGO
Density (g/cm³)	3.67	7.13
Effective atomic number	51	75
Index of refraction	1.85	2.15
Relative emission intensity	100	15
Peak wavelength (nm)	410	480
Decay constant (ns)	230	300
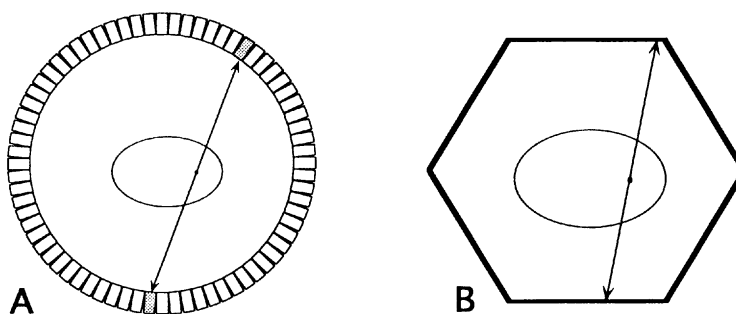
FIGURE 79.5 Representation of PET scanner geometries for typical scanners employing (A) multiple rings of small BGO scintillators, and (B) six large NaI(Tl) position-sensitive planar detectors. The arrows represent positron annihilation photons that are emitted 180° from each other and detected in opposing detectors. (Courtesy of Dr. T. Turkington.)

power of BGO is advantageous for detector designs that use smaller crystals with one-to-one PMTs, or position-encoded matrices of crystals [69]. The recently identified lutetium oxyorthosilicate (LSO) is a potential successor to BGO in detector block designs. LSO has a density of 7.4 g/mL, an effective atomic number of 59, a photofluorescent decay time of 40 ns, and light outputs that are ¾ that of NaI(Tl) [70].

PET Scanners

PET scanners use a number of different detector compositions and gantry configurations, each with its unique advantages and disadvantages [68]. Figure 79.5 shows two of the most common designs that are currently employed. At present, the majority of commercial designs employ a cylindrical geometry with individual BGO detector blocks arranged to form contiguous rings of detectors, each defining an image plane [71,72]. Most of these scanners have retractable lead (or tungsten) septa which are positioned between detector rings to attenuate photons that are emitted at angles not contained in the image plane. This minimizes the effect of out-of-plane scattered radiation, allowing accurate quantitation of the radioactivity distribution in each image plane by two-dimensional (tomographic) image reconstruction. With the septa retracted, all axial angles are accepted, allowing true three-dimensional volume imaging. Another scanner design uses large-area position-encoded NaI(Tl) detectors, allowing three-dimensional volume imaging [73]. In all cases, computer-assisted image reconstruction is used to produce quantitative images of radiotracer concentration in the body.

The spatial resolution of the radioactivity distributions seen in the PET image is primarily determined by the size of the detector elements. In scanners employing cylindrical detector geometry, the in-plane spatial resolution is highest in the center of the field of view (typically 4 to 5 mm FWHM of the point source response for present state-of-the-art scanners). The spatial resolution slowly degrades as the radius increases due to inadequate stopping of photons within incident detectors for nonperpendicular entrance angles. Likewise, the resolution in the axial direction is determined by the axial dimension of the detector elements.

79.7   Ultrasound Imaging

Ultrasound scanning provides a safe and noninvasive way to image the body. With this modality, brief pulses of sound are emitted by a transducer coupled to the skin surface. The sound pulse propagates through tissue at a fixed speed. Interfaces and other objects reflect portions of the acoustic energy back to the transducer, where they are detected as echoes. The ultrasound scanner forms one-dimensional, or more commonly two-dimensional, images of anatomic structures from the reflected echo patterns. In general imaging applications, ultrasound imaging uses frequencies in the 2 to 10 MHz range. Some newer ultrasound devices, for example, those used in emerging ophthalmology applications, use frequencies as high as 50 MHz [74,75].

Characteristics of Sound Waves in Tissue

The speed at which sound waves propagate through a medium depends on the density and compressibility of the medium. At 22℃, the speed of sound in air is around 300 m s^{-1}, while in fresh water it is 1480 m s^{-1}. Human soft tissues behave somewhat like water, with speeds of sound ranging from 1460 m s^{-1} for fat to 1620 m s^{-1} for muscle. The average speed of sound in tissue is taken to be 1540 m s^{-1} (1.54 mm/μs) [76,77].

Any interface, large or small, can reflect a fraction of the ultrasound energy and produce an echo. The relative amount of energy reflected depends on the change in density and compressibility at the interface; the greater the change in these properties of the materials forming the interface, the greater the amplitude of an echo. Examples of reflectors include organ boundaries, blood vessels, and small scatterers distributed more or less randomly throughout most organs. The majority of the echo data displayed on images can be attributed to this scattering process [77]. Shung [78] has reviewed experimental work on ultrasonic scattering vs. frequency in biological tissues.

As ultrasound pulses travel through tissue, they lose their strength due to attenuation. Attenuation is caused by scatter and reflection at interfaces and by absorption. For typical tissues, the amplitude of a 5-MHz beam decreases by about 50% for each centimeter traveled. The attenuation per unit distance is approximately proportional to the ultrasound frequency, so lower-frequency waves propagate greater distances through tissues than higher-frequency waves [79].

B-Mode Imagers

Figure 79.6 illustrates a typical configuration for an ultrasound imager. The operator places a handheld transducer on the skin surface of the patient. Early instruments utilized "single-element" transducers, but the majority of systems now use transducer arrays [80]. Acoustic pulses emitted by the transducer travel in well-defined beams. This beam can be "steered" in different directions, either mechanically with motors or electronically by using transducers arrays.

The same transducer detects echoes that arrive from interfaces in the body and applies them to the receiver, where they are amplified and processed for display. The instrument converts each echo signal into a dot on the display, the brightness of the dot being proportional to the echo amplitude at the transducer. The "scan converter" memory places dots in a location that corresponds to the reflector locations; information required to do this is the return time for each echo and the beam axis direction when the echo is detected.

The scanner constructs a cross-sectional image by sending out 100 to 200 such ultrasound beams, each in a slightly different direction, somewhat like a searchlight scanning the night sky. Echoes received from each beam direction are placed in the image memory using the scheme mentioned above. The entire image is updated at rates of 15 to 30 scans per second, producing a real-time image on the display monitor. This technique is referred to as B-mode imaging because echo signals simply modulate the intensity, or brightness, of the display at locations corresponding to their anatomic origin.
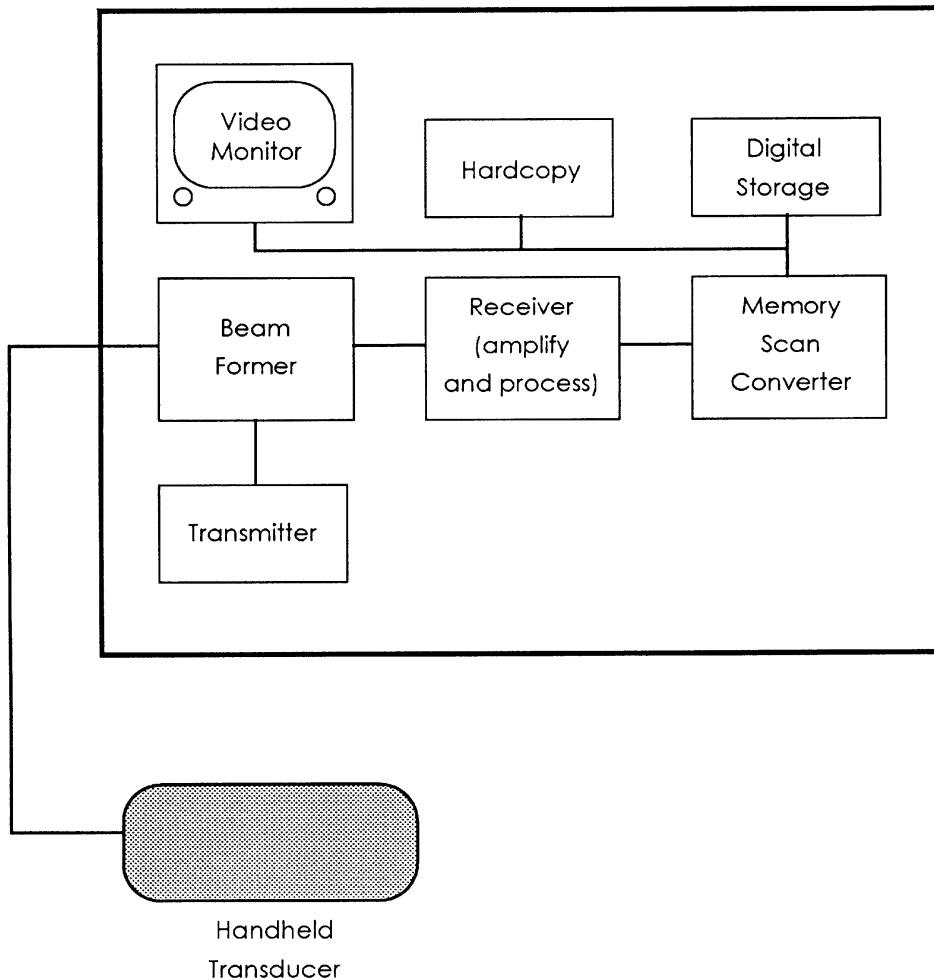
FIGURE 79.6   Components in a typical B-mode ultrasound device.

Doppler Techniques

Ultrasound instruments commonly provide Doppler records as well as B-mode images. Fundamentally, the Doppler effect is a change in the frequency of reflected waves when there is relative motion between the transducer and reflector. For motion directly toward or directly away from the transducer, the Doppler signal frequency f_d is given by

$$f_d = \frac{2 f_0 v}{c} \tag{79.7}$$

where f_0 is the frequency of the transmitted ultrasound, v is the velocity of the reflector, and c is the speed of sound. Thus, the Doppler signal frequency provides information on reflector velocity.

    Continuous wave (CW) Doppler instruments consist of a transducer with separate transmitting and receiving elements, a transmitter–receiver unit, and a signal display. They extract a Doppler signal from the complex echo pattern, usually by heterodyning the echo signal with a signal that is coherent with the transmitted wave, and then low pass filtering. The most common applications are to detect and measure

blood flow. With a 5-MHz ultrasound frequency and blood velocity of 50 cm/s, the Doppler signal frequency is 3.25 kHz, i.e., in the audible frequency range. A simple loudspeaker may be all that is necessary for interpreting the Doppler signal, but very often a real-time spectral analyzer is available.

Pulsed Doppler instruments are a bit more complicated, but allow the operator to define precisely the distance from the transducer from which Doppler signals are selected. In pulsed Doppler, an acoustic pulse is transmitted along a fixed beam line. Resultant echo signals are amplified and subjected to Doppler processing methods, similar to those outlined for the CW instrument. An operator-adjusted gate captures the waveform from the depth of interest, and a sample-hold device retains the value of this waveform until a subsequent pulse–echo sequence. Because the phase of the echo signal from moving reflectors changes from one pulse–echo sequence to the next, a Doppler signal can be constructed from the behavior over time of the sample-hold value.

Color Doppler Imaging

Color flow imagers may be thought of as extensions of pulsed Doppler machines. Rather than detecting Doppler signals from a single location, color flow imagers detect signals from all depths covered by the ultrasound beam, and for many beam directions. Most instruments extract and display the mean Doppler signal frequency for each location throughout the scanned field [81,82]. A color Doppler image is almost always combined with a B-mode image to provide both anatomic and flow data from the scanned plane.

Measurement of Ultrasound Instrument Performance

Defining "image quality" in ultrasound, and specifying quantifiable factors that relate to optimal B-mode imaging, is controversial to say the least. Important factors that are considered include spatial and contrast resolution, sensitivity, penetration depth, and geometric accuracy.

High-quality ultrasound imagers interrogate the scanned field using a sufficient number of individual beam lines (more than 100) such that gaps between lines can be ignored in resolution considerations. An exception may be in color flow imaging, where sparse line densities are needed for sufficient frame rates [77]. Thus, spatial resolution is dictated by the volume of the ultrasound pulse propagating through the tissue. The dimension of this pulse volume in the direction the pulse travels, i.e., the axial resolution, is determined by the duration of the pulse emitted by the transducer, while the dimension perpendicular to the beam axis, or the "lateral resolution" is determined by the beam width. Although ultrasound beam energy is concentrated near the axis, it is the nature of beams from finite-sized apertures that the intensity falls off gradually with increasing distance from the beam axis. Finally, the size of the ultrasound beam perpendicular to the image plane determines the "slice thickness," the width of the volume of tissue contributing to the echo data viewed in the image plane.

A variety of methods have been used for determining in-plane resolution. The lateral and axial dimensions of a reflector whose size is small enough that it can be considered a pointlike object are frequently used [83]. For a 3.5-MHz transducer, this "spot-size," can be as small as 0.7 mm in the axial dimension and 1 to 2 mm laterally. Smaller spot sizes are found with higher-frequency imagers, such as those using 10 MHz scan heads. Also, larger spot sizes are obtained with scanners that use fixed-focus, single-element transducers.

Slice thickness has been measured using a planar sheet of scatterers scanned with the ultrasound scanning plane intersecting the sheet at a 45° angle [83]. If the slice thickness were negligible, the image of the sheet in this projection would be a straight, horizontal line. The finite thickness of the scanned slice causes a thickening of the line; in fact, for the 45° orientation the vertical size of the image of the sheet corresponds to the slice thickness. For all ultrasound imaging systems, except annular array trans-ducers, the slice thickness is the worst measure of spatial resolution, ranging from the 10 mm to 2 to 3 mm, depending on depth, for a 3.5-MHz transducer.

Physicians commonly use ultrasound imagers to detect cancerous tumors, for which the echoes are slightly stronger or weaker than the surrounding region. "Contrast-detail" tests [84,85] measure the

smallest object that can be visualized at a fixed backscatter difference. Spherical mass detectability [86] assesses capabilities to visualize realistic focal lesions. Masses in the latter detection test are characteristic of actual tumors; furthermore, they are easily distributed throughout the scanning plane, assessing resolution at all depths.

Scanner sensitivity is an important performance feature, especially because spatial resolution can be enhanced with higher-frequency transducers. However, this is at the expense of increased ultrasound beam attenuation and poorer penetration. Although absolute measurements of sensitivity of scanners have been done [87], most centers rely upon clinically meaningful "maximum visualization distances" [83,88] for estimating and comparing sensitivity. Geometric accuracy also is important, as images frequently are used to determine structure dimensions, such as fetal head size when determining gestational age [89]. Calibration of distance measurements are done following standard protocols [83,90]; fortunately, modern scanners with digitally based image formation maintain their accuracy much better than previous systems, and many physicists maintain that tests for geometric accuracy are not crucial in routine performance assessments.

79.8   Magnetic Resonance Imaging (MRI)

Magnetic resonance (MR) imaging is a new medical imaging modality which uses magnetic fields and radiofrequency (RF) energy to produce images of the body. The technique is based on nuclear magnetic resonance (NMR) [91], which is a quantum mechanical phenomenon exhibited by atoms having either an odd number of protons or neutrons. Such atoms have a nonzero nuclear magnetic moment, μ, and will precess (or rotate) about an external magnetic field (B_0) with a frequency of $\omega_0 = \gamma \mathbf{B}_0$, where γ is the gyromagnetic ratio which for ^{1}H is 42.57 MHz/T. A number of isotopes (including ^{1}H, ^{31}P, ^{23}Na, ^{2}H) exhibit the NMR phenomena; however, the majority of MR scanners image ^{1}H. This is because, relative to other isotopes, ^{1}H has a high inherent sensitivity and abundance in tissue. Therefore, the following discussion is limited to ^{1}H MR imaging. When placed in a $\mathbf{B}_0$ field, ^{1}H nuclei align their spins either parallel or antiparallel to $\mathbf{B}_0$, with a slight excess in the lower energy parallel state. At $T = 25°C$ and $|\mathbf{B}_0| = 1.5$ T, an excess of ~5 in 10^6 atoms are in the parallel state (this excess increases with $\mathbf{B}_0$ and T^{-1}). Because there are ~10^{23} ^{1}H per milliliter of tissue, this excess, when summed over even a small volume, results in a net magnetization, $\mathbf{M} = \Sigma \mu$.

MR Imaging Techniques

The Bloch equations [91,92] are a set of phenomenological equations that succinctly describe the evolution of the net magnetization $\mathbf{M}(\mathbf{r},t)$ during an MR imaging experiment:

$$\frac{\partial \mathbf{M}(\mathbf{r},t)}{\partial t} = \gamma \mathbf{M}(\mathbf{r},t) \times \mathbf{B}(\mathbf{r},t) - \frac{M_x(t)\hat{x} + M_y\hat{y}}{T2} + \frac{\left(M_z(t) - M_0\right)\hat{z}}{T1} \qquad (79.8)$$

where $\mathbf{M}(\mathbf{r},t) = (M_x(t), M_y(t), M_z(t))$; M_0 is the initial (or equilibrium) magnetization, $\mathbf{B}(\mathbf{r},t) = \mathbf{B}_0 + \mathbf{G}(\mathbf{r},t) \cdot \mathbf{r} + \mathbf{B}_1(t)$ is the total applied magnetic field and includes terms representing the static field, $\mathbf{B}_0$, the field gradients, $\mathbf{G}(\mathbf{r},t) \cdot \mathbf{r}$; and the magnetic field component of any applied RF excitation, $\mathbf{B}_1(t)$; and T1 and T2 are the characteristic relaxation times of the tissues being imaged. The coordinate system is described in Figure 79.7. The $\mathbf{B}_0$ and $\mathbf{G}(\mathbf{r},t) \cdot \mathbf{r}$ fields are parallel to z, and the $\mathbf{B}_1$ field is orthogonal to z. Every MR imaging experiment consists of an excitation phase, in which the equilibrium magnetization is tipped away from z (the longitudinal axis) and into the transverse (x–y) plane. This is followed by a detection phase, in which the signal emitted by the excited spins is manipulated so that an echo forms. The echo-time (TE) and the repetition-time (TR) denote the time between excitation and echo formation,
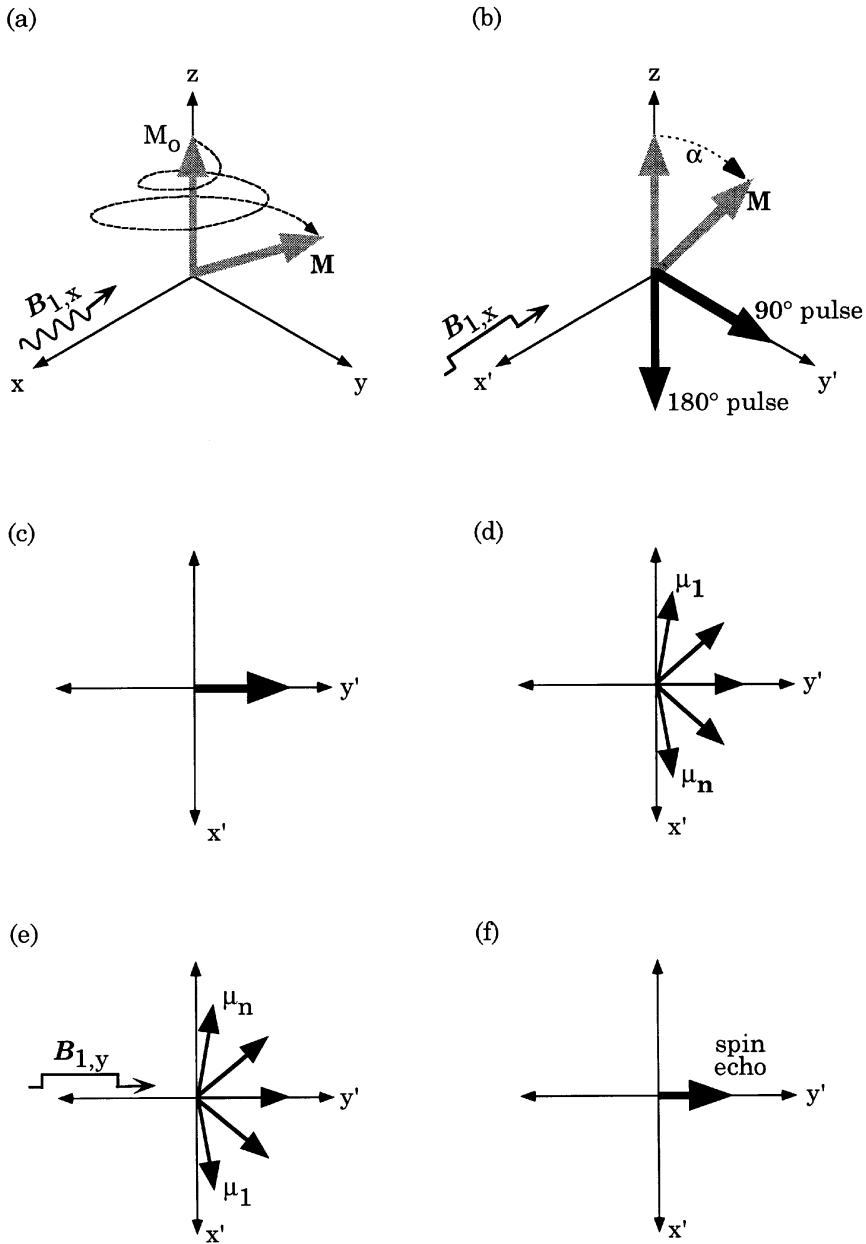
FIGURE 79.7 Graphical depiction of the MR imaging process showing the effect of the $\mathbf{B}_1$-excitation pulse (a–b) and formation of a spin-echo (c–f). In (a) an RF pulse, $\mathbf{B}_1$, is applied along the x axis causing the net magnetization to tip away from equilibrium, $\mathbf{M}_0$, as it precesses about z. Viewed in the rotating frame of reference, this corresponds to a nutation by some angle α in the $y'–z$ plane. After application of an $\alpha = 90°$ pulse, $\mathbf{M}$ lies in the $x'–y'$ plane (c) and is subject to variations in the local magnetic field which cause the individual spins to precess at different frequencies, i.e., μ_1 and μ_n in (d). The local field variations could be due to gradients or field inhomogeneity, the latter effect leading to T2* signal loss. By applying an $\alpha = 180°$ RF pulse along y', the spins are rotated about y' (e) and are refocussed into an echo (f).

and the time between successive excitation phases, respectively. Starting at equilibrium, RF energy at ω_0 is applied to create an oscillating $\mathbf{B}_1(t)$ field which tips $\mathbf{M}$ toward the transverse plane, at which time it begins to precess about z (Figure 79.7a). Viewed in a frame of reference rotating at $-\omega_0$ about z (x', y', z), the RF excitation corresponds to tipping $\mathbf{M}$ through an angle α from z (Figure 79.7b). Gradients, $\mathbf{G}(\mathbf{r},t)$, are then applied so that spatial information is encoded into the precessional frequency of $\mathbf{M}$, $\omega = \gamma[\mathbf{B}_0 + \mathbf{G}(\mathbf{r},t) \cdot \mathbf{r}]$. Additional gradients and/or RF-excitation pulses are used to refocus the magnetization into an echo (Figure 79.7c through f). The precessing transverse component of the magnetization ($M_{xy} = M_x + jM_y$) induces a signal (EMF) in the receiver coil, and this is recorded during echo formation. The experiment is repeated many times (normally 128 to 256) using predetermined gradient strengths [93] so that a complete data set is collected. These data are in spatial-frequency space (known as $\mathbf{k}$-space) and images are reconstructed after taking the multidimensional Fourier transform of $\mathbf{k}$-space [94]. Gradients can be used to encode spatial information along all axes, so either two-dimensional (planar) or three-dimensional (volume) imaging is possible with MR.

MR Image Contrast

Excited spins undergo two principal relaxation processes, spin–lattice and spin–spin relaxation. Spin–lattice relaxation occurs when spins lose energy to surrounding molecules and return to the equilibrium position, M_0. Spin–spin relaxation is due to local interactions which cause spins to precess at different rates, resulting in a reduction in $\mathbf{M}_{xy}$ (Figure 79.7d). Field inhomogeneity due to an imperfect magnet is reversible ($\delta\mathbf{B}(\mathbf{r})$), while inhomogeneity due to variations in local chemical structure is not. The relaxation times T1 and T2 characterize spin–lattice and spin–spin relaxation processes, respectively, and from the Bloch equation (Equation 79.8) the following equations can be derived for the relaxation of spins tipped by $\alpha = 90°$ at $t = 0$:

$$M_z\left(t\right) = M_0\left(1 - e^{-t/\text{T1}}\right) \;\; \text{and} \;\; M_{xy}\left(t\right) = M_{xy}\left(t = 0\right)e^{-t/\text{T2}} \tag{79.9}$$

Together with the differences in the inherent proton density between tissues, differences in T1 and T2 are the basis of the contrast seen in MR images. A spin-echo (SE) acquisition uses one or more additional RF excitations with $\alpha = 180°$ to refocus the reversible component of spin–spin relaxation so that one or more echoes are formed. Equation 79.9 shows that images with primarily T1 weighting, T2 weighting, or proton density weighting result when relative to T1 and T2: TR and TE are short, TR and TE are long, and TR is long and TE is short, respectively. In practice, images with a pure weighting are not obtainable because image contrast is due to a mixture of these contrast mechanisms. Gradient-recalled echo (GRE) imaging uses additional gradients, instead of an $\alpha = 180°$ pulse, to produce echoes and results in images with significantly shorter TR and TE than SE techniques. GRE images, however, do not refocus the reversible component of spin–spin relaxation and are thus susceptible to T2* signal loss, where $1/\text{T2*} = 1/\text{T2} + 2\pi\gamma|\delta\mathbf{B}(\mathbf{r})|$. This leads to lower signal-to-noise in GRE images compared with SE images. Since TR is short compared with T1, GRE images tend to have T1 weighting. If TE approaches T2*, then the T2* weighting becomes significant.

MR Instrumentation

The key components of a modern MR imaging system include a magnet, a pulse sequencer, gradient and shim coils, and an RF transmitter/receiver — the function of which are controlled by a host computer (Figure 79.8). To obtain the $\mathbf{B}_0$-field, most commercial scanners use superconducting magnets, although some special-purpose (and often lower-cost) scanners may use resistive magnets. Superconducting magnets generally have field strengths between 0.5 and 4.0 T, while resistive magnets normally have field strengths < 0.3 T. The improved signal-to-noise ratio obtained with superconducting designs is offset by the need for periodic cryogen replacement. More modern magnets, however, minimize this cost by including a cryogen reliquefier. Two sets of auxiliary gradient coils are located within the main magnet
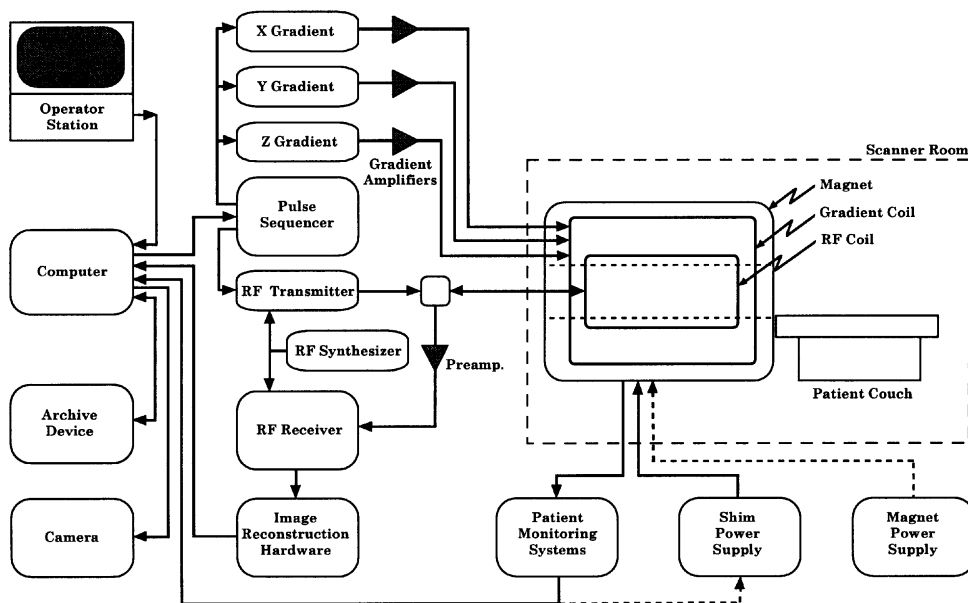
FIGURE 79.8 Overview of an MR scanner showing key components.

to provide spatially varying fields, $\mathbf{G}(\mathbf{r},t)$, and to allow shimming of the $\mathbf{B}_0$-field. Current gradient coil hardware can generate maximum gradients of up to 40 mT/m with rise times of 120 μs and allow fields of view from 4 to 48 cm. Shim coils improve the homogeneity of the $\mathbf{B}_0$ field by decreasing $\delta\mathbf{B}(r)$ to a few parts per million in order to minimize T2* effects and spatial distortions. Modern scanners incorporate a digital RF subsystem which excites the spins and then records the emitted signals via one or more RF coils within the magnet. An RF synthesizer is coupled to both the RF transmitter and receiver, so that synchronous detection is possible. The RF system is connected either to separate transmit and receive coil(s) or to a combined transmit/receive coil(s).

To acquire an MR image, the host computer interacts with the operator who defines the imaging parameters (such as α, TR and TE, slice location, and field of view). The parameters are then translated into instructions which are executed on a synchronous state machine known as a pulse sequencer. This device provides real-time control of the gradient and RF waveforms as well as other control functions, such as unblanking the RF receiver and enabling the ADC during an echo. Data are collected and demodulated by the receiver, and then images are reconstructed using specialized hardware built normally around a fast-array processor. The images are sent to the host computer for operator station display, archival or filming. In addition, many MR scanners incorporate devices for monitoring heart and respiration rate, and allow these signals to trigger or gate image acquisition. Future MR imaging systems will probably include higher $\mathbf{B}_0$-field and gradients, and faster data processing/reconstruction hardware. In addition to current imaging apparatus, it is likely that dedicated instruments will be increasingly used to study the heart and for performing neurofunctional imaging and MR-guided interventional procedures.

References

1. G. Revesz, H. L. Kundel, and M. A. Graber, The influence of structured noise on the detection of radiologic abnormalities, *Invest. Radiol.*, 9: 479–486, 1974.
2. A. Rose, *Vision: Human and Electronic,* New York: Plenum Press, 1973.
3. K. Doi, K. Strubler, and K. Rossmann, Truncation errors in calculating the MTF of radiographic screen-film systems from the line spread function, *Phys. Med. Biol.*, 17: 241–250, 1972.
4. Modulation Transfer Function of Screen-film Systems, ICRU Report 41, 1986.

5. H. Fujita, D.-Y. Tsai, T. Itoh, K. Doi, J. Morishita, K. Ueda, and A. Ohtsuka, A simple method for determining the modulation transfer function in digital radiography, *IEEE Trans. Med. Imag.*, 11: 34–39, 1992.

6. J. T. Dobbins III, D. L. Ergun, L. Rutz, H. Blume, D. A. Hinshaw, and D. C. Clark, DQE(f) of four generations of computed radiography acquisition devices, *Med. Phys.*, 22: 1581–1593, 1995.

7. J. M. Boone and J. A. Seibert, An analytical edge spread function model for computer fitting and subsequent calculation of the LSF and MTF, *Med. Phys.*, 21: 1541–1545, 1994.

8. J. M. Sandrik and R. F. Wagner, Absolute measures of physical image quality: measurement and application to radiographic magnification, *Med. Phys.*, 9: 540–549, 1982.

9. P. C. Bunch, R. Shaw, and R. L. van Metter, Signal-to-noise measurements for a screen-film system, *Proc. SPIE*, 454: 154–163, 1984.

10. P. C. Bunch, K. E. Huff, and R. van Metter, Analysis of the detective quantum efficiency of a radiographic screen-film combination, *J. Opt. Soc. Am.*, 4: 902–909, 1987.

11. J. T. Dobbins III, Effects of undersampling on the proper interpretation of modulation transfer function, noise power spectra and noise equivalent quanta of digital imaging systems, *Med. Phys.*, 22: 171–181, 1995.

12. M. L. Giger, K. Doi and C. E. Metz, Investigation of basic imaging properties in digital radiography. 2. Noise Wiener spectrum, *Med. Phys.*, 11: 797–805, 1984.

13. R. B. Blackman and J. W. Tukey, *The Measurement of Power Spectra,* New York: Dover, 1958.

14. R. F. Wagner and J. M. Sandrik, An introduction to digital noise analysis, in A. G. Haus, Ed., *The Physics of Medical Imaging: Recording System Measurements and Techniques*, New York: American Association of Physicists in Medicine, pp. 524–545, 1979.

15. G. T. Barnes, Radiographic mottle: a comprehensive theory, *Med. Phys.*, 9: 656–667, 1982.

16. R. F. Wagner, Fast Fourier digital quantum mottle analysis with application to rare Earth intensifying screen systems, *Med. Phys.*, 4: 157–162, 1977.

17. H. H. Barrett and W. Swindell, *Radiological Imaging*. New York: Academic Press, 1981.

18. G. M. Jenkins and D. G. Watts, *Spectral Analysis and Its Applications*, San Francisco, CA: Holden-Day, 1968.

19. K. Koedooder, J. Strackee, and H. W. Venema, A new method for microdensitometer slit length correction of radiographic noise power spectra, *Med. Phys.*, 13: 469–473, 1986.

20. M. L. Giger and K. Doi, Investigation of basic imaging properties in digital radiography. 1. Modulation transfer function, *Med. Phys.*, 11: 287–295, 1984.

21. J. T. Bushberg, J. A. Seibert, E. M. Leidholdt, Jr., and J. M. Boone, *The Essential Physics of Medical Imaging*, Baltimore, MD: Williams & Wilkins, 1994.

22. M. Braun and B. C. Wilson, Comparative evaluation of several rare-Earth film-screen systems, *Radiology*, 144: 915–919, 1982.

23. M. Sonoda, M. Takano, J. Miyahara, and H. Kato, Computed radiography utilizing scanning laser stimulated luminescence, *Radiology*, 148: 833–838, 1993.

24. W. Hillen, U. Schiebel, and T. Zaengel, Imaging performance of a digital storage phosphor system, *Med. Phys.*, 14: 744–751, 1987.

25. H. Blume, Stimulable phosphor systems—technical aspects. In W. W. Peppler and A. Alter, Eds., *Proc. Chest Imaging Conf '87,* University of Wisconsin, Madison, pp. 194–201, 1987.

26. U. Neitzel, I. Maack, and S. Günther-Kohfahl, Image quality of a digital chest radiography system based on a selenium detector, *Med. Phys.*, 21: 509–516, 1994.

27. C. H. Slump, G. J. Laanstra, H. Kuipers, M. A. Boer, A. G. J. Nijmeijer, M. J. Bentum, R. Kemner, H. J. Meulenbrugge, and R. M. Snoeren, Image quality characteristic of a novel X-ray detector with multiple screen-CCD sensors for real-time diagnostic imaging. *Proc. SPIE*, 3032: 60–71, 1997.

28. L. E. Antonuk, Y. El-Mohri, J. H. Siewerdsen, J. Yorkston, W. Huang, V. E. Scarpine, and R. A. Street, Empirical investigation of the signal performance of a high-resolution, indirect detection, active matrix flat panel imager (AMFPI) for fluoroscopic and radiographic operation, *Med. Phys.*, 24: 51–70, 1997.

29. D. L. Lee, L. K. Cheung, and L. S. Jeromin, A new digital detector for projection radiography, *Proc. SPIE*, 2432: 237–249, 1995.

30. D. P Boyd, R. G. Gould, J. R. Quinn, R. Sparks, J. H. Stanley, and W. B. Herrmannsfeldt, A proposed dynamic cardiac densitometer for early detection and evaluation of heart disease, *IEEE Trans. Nucl. Sci.*, 26: 2724–2727, 1979.

31. C. H. McCollough and R. L. Morin, The technical design and performance of ultrafast computed tomography, *Radiol. Clin. North Am.,* 32: 521–536, 1994.

32. P. M. Silverman, C. J. Cooper, D. I. Weltman, and R. K. Zeman, Helical CT: practical considerations and potential pitfalls, *Radiographics*, 15(1): 25–36, 1995.

33. J. Hsieh, A general approach to the reconstruction of X-ray helical computed tomography, *Med. Phys.*, 23: 221–229, 1996.

34. J. Radon, On the determination of functions from their integrals along certain manifolds, *Ber. Verh. Sächs. Akad. Wiss. Leipzig, Math. Phys. Kl.*, 69: 262–277, 1917.

35. A. C. Kak and M. Slaney, *Principles of Computerized Tomographic Imaging,* New York: IEEE Press, 1988.

36. E. C. McCullough, J. T. Payne, H. L. Baker, Jr., R. R. Hattery, P. F. Sheedy, D. H. Stephens, and E. Gedgaudus, Performance evaluation and quality assurance of computed tomography scanner, with illustrations from the EMI, ACTA, and Delta scanners, *Radiology*, 120: 173–188, 1976.

37. E. C. McCullough and J. T. Payne, X-ray-transmission computed tomography, *Med. Phys.*, 4: 85–98, 1977.

38. R. T. Droege and R. L. Morin, A practical method to measure the MTF of CT scanners, *Med. Phys.*, 9: 758–760, 1982.

39. H. N. Wagner, Jr., Z. Szabo, and J. W. Buchanan, Eds., *Principles of Nuclear Medicine*, 2nd ed., Philadelphia, PA: Saunders, 1995.

40. M. P. Sandler, Ed., *Diagnostic Nuclear Medicine*, 3rd ed., Baltimore, MD: Williams & Wilkins, 1996.

41. R. Chandra, *Introductory Physics of Nuclear Medicine,* 4th ed., Philadelphia, PA: Lea & Febiger, 1992.

42. J. A. Sorenson and M. E. Phelps, *Physics in Nuclear Medicine*, 2nd ed., Orlando, FL: Grune & Stratton, 1987.

43. J. L. Littlefield and T. G. Rudd, [99mTc]-hydroxymethylene diphosphonate and [99mTc]-methylene diphosphonate biologic and clinical comparison: concise communication, *J. Nucl. Med.,* 24: 643, 1983.

44. G. B. Saha, W. J. MacIntyre, R. C. Brunken, R. T. Go, S. Raja, C. O. Wong, and E. Q. Chen, Present assessment of myocardial viability by nuclear imaging, *Semin. Nucl. Med.*, 26 (4): 315–35, 1996.

45. T. R. Miller and J. W. Wallis, Cardiac nuclear medicine, *Curr. Probl. Diagn. Radiol.*, 17 (5): 157–193, 1988.

46. R. J. Boudreau and M. K. Loken, Functional imaging of the heart, *Semin. Nucl. Med.*, 17(1): 28–38, 1987.

47. F. J. Wackers, D. S. Berman, J. Maddahi, D. D. Watson, G. A. Beller, H. W. Strauss, C. A. Boucher, M. Picard, B. L. Holman, and R. Fridrich, Technetium-99m hexakis 2-methoxyisobutyl isonitrile: human biodistribution, dosimetry, safety, and preliminary comparison to thallium-201 for myocardial perfusion imaging, *J. Nucl. Med.*, 30: 301–311, 1989.

48. B. M. W. Tsui, X. Zhao, E. C. Frey, and W. H. McCartney, Quantitative single-photon emission computed tomography: basics and clinical considerations, *Semin. Nucl. Med.*, 24: 38–65, 1994.

49. J. Caldwell, D. Williams, G. Harp, J. Stratton, and J. Ritchie, Quantitation of size of relative perfusion defect by single-photon emission computed tomography, *Circulation,* 70: 1048–1056, 1984.

50. Performance Measurements of Scintillation Cameras, Standards Publication No. NU1-1980, Washington D.C.: National Electrical Manufacturers Association, 1980.

51. G. Muehllehner, R. H. Wake, and R. Sano: Standards for performance measurements in scintillation cameras, *J. Nucl Med.,* 22: 72–77, 1981.

52. Scintillation Camera Acceptance Testing and Performance Evaluation, AAPM Report No. 6, New York: American Association of Physicists in Medicine, 1980.

53. Computer-Aided Scintillation Camera Testing and Performance Evaluation, AAPM Report No. 9, New York: American Association of Physicists in Medicine, 1987.

54. Performance Measurements of Scintillation Cameras, Standards Publication No. NU 1-1986, Washington D.C.: National Electrical Manufacturers Association, 1986.

55. Guide to Revised Standards for Performance Measurements of Scintillation Cameras, Washington D.C.: National Electrical Manufacturers Association, 1986.

56. L. S. Graham, Quality assurance of Auger cameras, in D. V. Rao, R. Chandra, and M. C. Graham, Eds., *Physics of Nuclear Medicine Recent Advances,* Monograph 10 of the American Association of Physicists in Medicine (AAPM); New York: American Institute of Physics, pp. 68–82, 1984.

57. L. A. O'Tuama and S. T. Treves, Brain single-photon emission computed tomography for behavior disorders in children, *Semin. Nucl. Med.,* 23 (3): 255–264, 1993.

58. G. B. Saha, W. J. MacIntyre, and R. T. Go, Radiopharmaceuticals for brain imaging, *Semin. Nucl. Med.,* 24 (4): 324–349, 1994.

59. S. Steien and J. Aaseth, Thallium-201 as an agent for myocardial imaging studies, *Analyst,* 120 (3): 779–781, 1995.

60. A. Taylor, Jr. and J. V. Nally, Clinical applications of renal scintigraphy, *Am. J. Roentgenol.,* 164: 31–41, 1995.

61. R. Schlosser and S. Schlegel, D2-receptor imaging with [123I]IBZM and single photon emission tomography in psychiatry: a survey of current status, *J. Neural Transm. Gen. Sect.,* 99 (1–3): 173–185, 1995.

62. T. Sunderland, G. Esposito, S. E. Molchan, R. Coppola, D. W. Jones, J. Gorey, J. T. Little, M. Bahro, and D. R. Weinberger, Differential cholinergic regulation in Alzheimer's patients compared to controls following chronic blockade with scopolamine: a SPECT study, *Psychopharmacology,* 121 (2): 231–241, 1995.

63. B. Shapiro, J. C. Sisson, B. L. Shulkin, M. D. Gross, and S. Zempel, The current status of meta-iodobenzylguanidine and related agents for the diagnosis of neuro-endocrine tumors, *Q. J. Nucl. Med.,* 39 (4 Suppl. 1): 3–8, 1995.

64. B. Shapiro, Imaging of catecholamine-secreting tumours: uses of MIBG in diagnosis and treatment, *Baillieres Clin. Endocrinol. Metabol.,* 7 (2): 491–507, 1993.

65. M. P. Stokkel, B. M. Kwa, and E. K. Pauwels, Imaging and staging of small-cell lung cancer: is there a future role for octreotide scintigraphy? *Br. J. Clin. Pract.,* 49: 235–238, 1995.

66. E. P. Krenning, D. J. Kwekkeboom, J. C. Reubi, P. M. Van Hagen, C. H. van Eijck, H. Y. Oei, and S. W. Lamberts, [111In]-octreotide scintigraphy in oncology, *Metab. Clin. Exp.,* 41 (9 Suppl. 2): 83–86, 1992.

67. E. J. Hoffman and M. E. Phelps, Positron emission tomography: principles and quantitation, in M. Phelps, J. Mazziotta, and H. Schelbert, Eds., *Positron Emission Tomography and Autoradiography: Principles and Applications for the Brain and Heart,* New York: Raven Press, pp. 237–286, 1986.

68. R. A. Koeppe and G. D. Hutchins, Instrumentation for positron emission tomography: tomograph and data processing and display systems, *Semin. Nucl. Med.,* 22 (3): 162–181, 1992.

69. M. E. Casey and R. Nutt, A multicrystal two dimensional BGO detector system for positron emission tomography, *IEEE Trans. Nucl. Sci.,* NS-33: 460–463, 1986.

70. C. L. Melcher and J. S. Schweitzer, Cerium-doped lutetium oxyorthosilicate: a fast, efficient new scintillator, in *Abstracts of Papers Presented at IEEE Nuclear Science Symposium,* Santa Fe, NM, November, 1991 (Abstract).

71. K. Wienhard, M. Dahlbom, L. Eriksson, C. Michel, T. Bruckbauer, U. Pietrzyk, and W. D. Heiss, The ECAT EXACT HR: performance of a new high resolution positron scanner, *J. Comput. Assist. Tomogr.,* 18: 110–118, 1994.

72. T. R. DeGrado, T. G. Turkington, J. J. Williams, C. W. Stearns, J. M. Hoffman, and R. E. Coleman, Performance characteristics of a whole body PET scanner, *J. Nucl. Med.,* 35: 1398–1406, 1994.

73. J. A. Karp, G. Muehllehner, D. A. Mankoff, C. E. Ordonez, J. M. Ollinger, M. E. Daube-Witherspoon, A. T. Haigh, and D. J. Beerbohm, Continuous-slice PENN-PET: a positron tomograph with volume imaging capability, *J. Nucl. Med.,* 31: 617–627, 1990.

74. C. J. Pavlin, K. Harasiewicz, M. D. Sherar, and F. S. Foster, Clinical use of ultrasound biomicroscopy, *Ophthalmology,* 98: 287–295, 1991.

75. D. H. Turnbull, High frequency ultrasound imaging, in L. Goldman and J. B. Fowlkes, Eds., *Medical CT and Ultrasound, Current Technology and Applications,* Madison, WI: Advanced Medical Publishing, pp. 285–297, 1995.

76. P. N. T. Wells, Propagation of ultrasound waves through tissue, in G. D. Fullerton and J. A. Zagzebski, Eds., *Medical Physics of CT and Ultrasound: Tissue Imaging and Characterization*, AAPM Monograph 6, College Park, MD American Association of Physicists in Medicine, pp. 367–387, 1980.

77. J. A. Zagzebski, *Essentials of Ultrasonic Physics,* St. Louis, MO: Mosby, 1996.

78. K. Shung, *In vitro* experimental results on ultrasonic scattering in biological tissues, in K. Shung and G. Thieme, Eds., *Ultrasonic Scattering in Biological Tissues*, Boca Raton, FL: CRC Press, pp. 291–312, 1993.

79. M. Insana, Sound attenuation in tissue, in L. Goldman and J. B. Fowlkes, Eds., *Medical CT and Ultrasound, Current Technology and Applications,* Madison, WI: Advanced Medical Publishing, pp. 15–33, 1995.

80. D. H. Turnbull, Fundamentals of Acoustic Transduction, in L. Goldman and J. B. Fowlkes, Eds., *Medical CT and Ultrasound, Current Technology and Applications,* Madison, WI: Advanced Medical Publishing, pp. 49–66, 1995.

81. K. Ferrara and G. DeAngelis, Color flow mapping, *Ultrasound Med. Biol.*, 23(3): 321–345, 1997.

82. K. J. W. Taylor, P. N. Burns, and P. N. T. Wells*, Clinical Application of Doppler Ultrasound*, 2nd ed., New York: Raven Press, pp. 19–34; 55–94, 1995.

83. *Standard Methods for Measuring the Performance of Pulse Echo Ultrasound Imaging Equipment*, Laurel, MD: American Institute of Ultrasound in Medicine, 1991.

84. H. Lopez, M. H. Loew, P. F. Butler, M. C. Hill, and R. M. Allman, A clinical evaluation of contrast-detail analysis for ultrasound images, *Med. Phys.*, 17: 48–57, 1993.

85. *Methods for Measuring Performance of Pulse-Echo Ultrasound Equipment- Part II: Digital Methods*, Laurel, MD: American Institute of Ultrasound in Medicine, 1995.

86. J. J. Rownd, E. L. Madsen, J. A. Zagzebski, G. R. Frank, and F. Dong, Phantoms and automated system for testing the resolution of ultrasound scanners, *Ultrasound Med. Biol.*, 23(2): 245–260, 1997.

87. *Standard Specification of Echoscope Sensitivity and Noise Level Including Recommended Practice For Such Measurements,* Laurel, MD: American Institute of Ultrasound in Medicine, 1991.

88. *Quality Assurance Manual for Gray Scale Ultrasound Scanners,* Laurel, MD: American Institute of Ultrasound in Medicine, 1995.

89. C. M. Rumack, S. R. Wilson, and J. W. Charboneau, *Diagnostic Ultrasound,* 2nd ed., St. Louis, MO: Mosby, 1997.

90. P. L. Carson and M. M. Goodsitt, Pulsed echo acceptance and quality control testing. In L. Goldman and J. B. Fowlkes, Eds., *Medical CT and Ultrasound, Current Technology and Applications,* Madison, WI: Advanced Medical Publishing, pp. 155–196, 1995.

91. C. P. Slichter, *Principles of Magnetic Resonance,* Berlin: Springer-Verlag, 1980.

92. F. Bloch, Nuclear induction, *Phys. Rev.*, 70: 460–485, 1946.

93. W. A. Edelstein, J. M. S. Hutchinson, G. Johnson, and T. Redpath, Spin-warp imaging and applications in whole body imaging, *Phys. Med. Biol.*, 25: 751–756, 1980.

94. W. S. Hinshaw and A. H. Lent, An introduction to NMR imaging: From Bloch equation to the imaging equation, *Proc. IEEE,* 71: 338–350, 1983.

Further Information

R. N. Bracewell, *The Fourier Transform and Its Applications*, 2nd ed., New York: McGraw-Hill, 1978.

E. O. Brigham, *The Fast Fourier Transform,* Englewood Cliffs, NJ: Prentice-Hall, 1974.

M. A. Brown and R. C. Semelka, *MRI: Basic Principles and Applications,* New York: Wiley-Liss, 1995.

J. C. Dainty and R. Shaw, *Image Science,* New York: Academic Press, 1974.

E. Fukushima and S. B. W. Roeder, *Experimental Pulse NMR. A Nuts and Bolts Approach,* Reading, MA: Addison-Wesley, 1981.

H. K. Huang, *Elements of Digital Radiology,* Englewood Cliffs, NJ: Prentice-Hall, 1987.

A. Macovski, *Medical Imaging Systems,* Englewood Cliffs, NJ: Prentice-Hall, 1983.

P. Sprawls and M. J. Bronskill, Eds., *The Physics of MRI:* 1992 *AAPM Summer School Proceedings,* Woodbury, NY: American Association of Physicists in Medicine, 1993. [An excellent overview of current MR instrumentation and clinical applications written by experts in the field.]